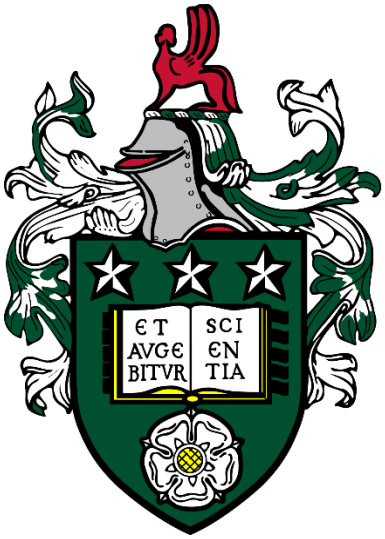

DEVELOPMENT OF AN ACTIVE CONTROL SYSTEM FOR A CANARD CONTROLLED SOUNDING ROCKET

Theodore Youds

School of Mechanical Engineering

University of Leeds

May 2023

MECH5080M Team Project

Author(s) Name: Theodore Youds

SID: 201230040

Supervisor(s) Name: Dr Jongrae Kim

Examiner Name: Dr Greg de Boer

Date of Submission: 03-05-2023

Development of an Active Control System for a Canard Controlled Rocket

UNIVERSITY OF LEEDS

SCHOOL OF MECHANICAL ENGINEERING

MECH5080M TEAM PROJECT 45 credits

TITLE OF PROJECT

Development of an Active Control System for a Canard Controlled Rocket

PRESENTED BY Theodore Youds

OBJECTIVES OF PROJECT

1. Create a mathematical model of the system dynamics from first principles.
2. Implement this model in Simulink in order to predict the behaviour of the system.
3. Design a controller that can deflect the canards in order to maintain more vertical flight.

IF THE PROJECT IS INDUSTRIALLY LINKED TICK THIS BOX AND PROVIDE DETAILS BELOW ×

COMPANY NAME AND ADDRESS:

Collins Aerospace

Wolverhampton

WV10 7EH

THIS PROJECT REPORT PRESENTS OUR OWN WORK AND DOES NOT CONTAIN ANY UNACKNOWLEDGED WORK FROM ANY OTHER SOURCES.

SIGNED *Theodore Youds* DATE *3rd May 2023*

Table of Contents

Acknowledgements

Firstly, I would like to acknowledge my Aptos teammates Ben, Joe, Liam, and Jordan. The achievements of this project speak for themselves, and it has been a pleasure working with you. Next, I would like to thank our supervisor Dr Jongrae Kim for his support of the project, as well the other academic staff within the School of Mechanical Engineering, especially Dr Greg de Boer and Dr Bilal Kaddouh.

We wouldn't have been able to conduct any flight testing without approval and mentoring from the UK Rocketry Association. Thank you to Colin Rowe, Chris Brown, and Paul Carter for your advice and guidance with all of LURA's rocketry endeavours. I am also extremely grateful for John Bonsor up at the Fairlie Moor Rocketry Site in Scotland. John has always been an advocate for LURA and allowed us to use his range to conduct preliminary flight tests in April 2023. His friendly, caring nature helped make both launch days an incredibly enjoyable process.

Finally, I would like to thank my girlfriend Katy, my parents, my housemates, friends, and family. You have supported me through everything over the past four years at the University of Leeds and I wouldn't have been able to do this without you. Thank you.

Abstract

Project Aptos aimed to develop a modular, canard controlled active stability system for a sounding rocket. This report focuses specifically on the development of the control algorithms used to command the system. An introduction to the project aims and objectives is given, specifically relating to the key stakeholders in the project: the Leeds University Rocketry Association (LURA) and Collins Aerospace. Relevant literature is discussed and existing work on control systems for orbital rockets, sounding rockets, and missile systems is drawn upon.

A three degree of freedom rotational model of a canard-controlled sounding rocket is derived and subsequently modelled using MATLAB and Simulink. These equations of motion are linearised using first order Taylor series techniques and small angle approximations, and a linear quadratic regulator (LQR) system is designed to control the rocket's attitude during ascent.

A separate PID controller is implemented to improve the performance of servomotor position control such that it meets the system requirements. The MATLAB System Identification app is then used to fit a transfer function model to the servomotor step response data, allowing for accurate modelling within Simulink.

The control system's performance is analysed, and it is proven that performance is sufficient for test flights to commence. The system's robustness is investigated over a range of expected variations in the rocket's geometry using a Monte Carlo approach. Finally, the Chernoff bound is applied in order to prove 95% accuracy and confidence in the system's performance and stability robustness.

Nomenclature

Symbols

α	Angle of attack
A_{ref}	Reference area (rocket cross-sectional area)
B	Body frame of reference
β	Sideslip angle
C_1	Corrective moment coefficient
C_2	Damping moment coefficient
C_{d_p}	Roll damping moment coefficient derivative w.r.t roll rate
$C_{N_{\alpha_0}}$	Normal force coefficient derivative of fin 2D aerofoil
C_{N_α}	Normal force coefficient derivative w.r.t. angle of attack
C_L	Lift coefficient
C_{L_α}	Lift coefficient derivative w.r.t angle of attack
d_{body}	Body tube diameter
$\mathbf{d}$	Disturbance vector, $\{\alpha \quad \beta\}^T$
δ	Robustness analysis confidence = $1 - \delta$
ϵ	Robustness analysis accuracy
F	Canard lift force, e.g. F_{x_1} for canard x_1
G	Global frame of reference
I_n	$n \times n$ identity matrix
J_R	Radial mass moment of inertia
J_L	Longitudinal mass moment of inertia
J	Mass moment of inertia matrix, $\{J_R \quad J_L \quad J_L\}^T \cdot \mathrm{I}_3$
K	LQR gain matrix
K_p	Proportional gain (PID controller)
K_i	Integral gain (PID controller)
K_d	Derivative gain (PID controller)
L_{damp}	Damping moment about roll axis
L_{can}	Moment induced by the canards about the roll axis
L_α	Canard roll moment derivative w.r.t angle of attack on canard
L/D	Lift to drag ratio
M_{corr}	Corrective moment about pitch axis
M_{damp}	Damping moment about pitch axis
M_{can}	Moment induced by the canards about the pitch axis
M_α	Canard pitch moment derivative w.r.t angle of attack on canard

$\dot{m}$	Engine exhaust gas mass flow rate
$\mathbf{M}$	Resultant moment vector
N_{corr}	Corrective moment about yaw axis
N_{damp}	Damping moment about yaw axis
N_{can}	Moment induced by the canards about the yaw axis
N_{α}	Canard yaw moment derivative w.r.t angle of attack on canard
N	Number of fins
N	Chernoff bound number of samples
ϕ	Roll angle
θ	Pitch angle
ψ	Yaw angle
p	Roll rate
q	Pitch rate
r	Yaw rate
ρ	Air density
$\bar{q}$	Dynamic pressure
Q	State-cost weighted matrix
R	Input-cost weighted matrix
$\sum c_i \xi_i^2 \Delta\xi_i$	Roll damping fin planform sum term (Niskanen, 2009)
S	Canard planform area
$\mathbf{u}$	Input vector, $\{x_1 \quad x_2 \quad y_1 \quad y_2\}^T$
v	Velocity
$\boldsymbol{\omega}$	Attitude rate vector, $\{p \quad q \quad r\}^T$
$\dot{\boldsymbol{\omega}}$	Attitude acceleration vector, $\{\dot{p} \quad \dot{q} \quad \dot{r}\}^T$
x_B, y_B, z_B	x, y, and z coordinates in the body frame of reference
x_G, y_G, z_G	x, y, and z coordinates in the global frame of reference
x_1, x_2	Pitch axis canard deflections
y_1, y_2	Yaw axis canard deflections
X_{CP}	Distance from nose cone tip to centre of pressure
X_{CG}	Distance from nose cone tip to centre of gravity
$\bar{X}_{CP}$	Distance between CP and CG, $X_{CP} - X_{CG}$
X_T	Distance from nose cone tip to nozzle throat
$\bar{X}_T$	Distance between CG and nozzle throat, $X_T - X_{CG}$
$X_{CP_{can}}$	Distance from nose cone tip to canard CP
$\bar{X}_{CP_{can}}$	Distance between CG and canard CP, $X_{CP_{can}} - X_{CG}$
$\mathbf{x}$	State vector, $\{\phi \quad \theta \quad \psi \quad p \quad q \quad r\}^T$
$\dot{\mathbf{x}}$	State derivative vector, $\{p \quad q \quad r \quad \dot{p} \quad \dot{q} \quad \dot{r}\}^T$
A, B, C, D, E, F	State space matrices

$Y_{CP_{can}}$	Distance from body frame origin to canard CP in y_B direction
$\bar{Y}_{CP_{can}}$	Distance between CG and canard CP in y_B direction, $Y_{CP_{can}} - Y_{CG}$
$Z_{CP_{can}}$	Distance from body frame origin to canard CP in z_B direction
$\bar{Z}_{CP_{can}}$	Distance between CG and canard CP in z_B direction, $Z_{CP_{can}} - Z_{CP}$

Acronyms

CFD	Computational fluid dynamics
CG	Centre of gravity
CP	Centre of pressure
LQR	Linear quadratic regulator (controller)
LURA	Leeds University Rocketry Association
MIMO	Multi-input, multi-output
PID	Proportional-integral-derivative (controller)
RAM	Random access memory
SISO	Single-input, single-output
SM	Static margin

1 Introduction

1.1 Project Aptos

This report forms part of the wider Project Aptos. Conducted as a five-person master's team project at the University of Leeds, Project Aptos aims to develop an active control system to improve the dynamic stability of a sounding rocket and ensure it flies a more vertical trajectory.

This project was run in conjunction with the Leeds University Rocketry Association (LURA) and was sponsored by Collins Aerospace. LURA aims to use the findings of this project to further develop the team's understanding of active control and will use future iterations of the Aptos system to ensure their rockets fly vertically, and therefore reach higher altitudes, in the pursuit of the UK amateur rocketry altitude record (UKRA, 2021).

Following consideration of different control systems, it was decided to use a set of four canards near the nose of the rocket controlled by servomotors to steer the rocket during ascent. Details of the full system, including the Pathfinder rocket on which the control system was implemented, are discussed by Youds et al. (2023).

1.2 Individual Aims and Objectives

This report discusses the design, analysis, and testing of the Aptos control algorithm. The aim of this project was to develop a closed loop controller capable of making the rocket fly a more vertical trajectory by controlling the deflections of the four canards.

This aim consisted of several objectives:

1. Create a mathematical model of the system dynamics from first principles.
2. Implement this model in Simulink in order to predict the behaviour of the system.
3. Design a controller that can deflect the canards in order to maintain more vertical flight.

1.3 Report Structure

These objectives are addressed in order through this report. First, existing literature on rocket active control systems is reviewed in Chapter 2. A mathematical model of the aerodynamic behaviour of the rocket is derived in Chapter 3, and this is then used to design a closed loop controller in Chapter 4. The position control of the servomotors is also discussed here. Chapter 4 concludes with analysis of the system's performance and robustness to expected variations in the rocket's geometry.

2 Literature Review and Theoretical Background

2.1 Sounding Rocket Stability

A rocket is considered passively stable if its centre of pressure (CP) is further aft than its centre of gravity (CG), such that the aerodynamic forces acting on the airframe keep the rocket aligned with the incoming airflow (NAROM Andøya Space Centre, 2018). It is generally accepted that a rocket must maintain a static margin, $SM > 1$, to be passively stable, where the static margin is given by the distance between the CP and the CG divided by the rocket's body diameter.

Passive stability is not always desirable, especially when a rocket aims to reach high altitudes. As identified by Uselton (1971) and Ujjin et al. (2021), passively stable rockets 'weathercock' in the presence of a crosswind. Whilst not flying vertically, the horizontal component of the thrust vector is effectively wasted, limiting altitude and increasing the possible landing radius (Lorenz and Bierig, 2013). What is more desirable for such rockets is an active system, which maintains dynamic stability and allows passively unstable rockets to fly pre-determined trajectories.

Active aerodynamic control surfaces can be used to steer rockets in a similar fashion to conventional aircraft. Their use is widely documented on missile and artillery systems, for example by Guo et al. (2016), Uselton (1971) and Seaberg and Smith (1951), where they are generally used for precise impacts. Despite the different use case, some control laws designed for weapon systems can be applied to sounding rockets.

Mracek and Ridgely (2006), for example, discuss at depth the autopilot system for a canard-controlled missile. Their system has great similarities with the system developed in this project, but the missile uses two sets of control surfaces: canards and rear fins.

Similar research exists for non-military rockets, although it generally focuses on larger-scale vehicles than Pathfinder. Choi and Bang (2000) developed an adaptive controller specifically for a slender sounding rocket, where the body-bending vibration of the airframe is considered and compensated for by the controller. Despite the similarities between Pathfinder and the KSR-II rocket examined in the paper, this level of structural analysis is not required for this project, where the fibreglass airframe provides good rigidity relative to the low thrust and aerodynamic loads.

Braswell et al. (2017) discuss the development of a canard control system as a payload for the NASA Student Launch Competition. A series of flight tests were performed to tune the controller, though a loose fin on the competition flight prevented the system

from performing as expected. The scale of the rocket itself is not dissimilar to Pathfinder and the budget and timescales align well with this project, though their system focusses solely on controlling roll, in contrast to the three-axis control needed for Aptos.

2.2 Closed Loop Control Systems

These papers provide a good insight into different control law options. Since Braswell et al. (2017) aim to control roll attitude only, the system is single-input, single-output (SISO), and thus a PID controller is used. This controller is simple to setup and tuning it does not require a linear model of the system, though the effects of the gain values themselves are not always intuitive for more complex nonlinear systems.

Another option is an LQR, as implemented by Mracek and Ridgely (2006). LQR controllers are inherently robust, handle multi-input, mutli-output (MIMO) systems very well, and are intuitive to tune. Actuating both the canards and rear fins introduces additional complexity in Mracek and Ridgely's work, though their strategy for tuning and analysing the system's performance was useful for this project. Aside from rockets, discussion of various control systems for quadrotor drones (Vigneswaran and Kp, 2019) and satellites (Narkiewicz et al., 2020) also provided helpful research for this project.

2.3 Robustness Analysis

Variations in the rocket's geometry and mass properties occur during the manufacturing process and therefore in reality, the system dynamics will differ from the model that the controller has been designed with. It is therefore important to verify that a controller is robust to these variations in terms of stability and performance.

Robustness and stability can be investigated by examining the worst perturbation from the nominal state space in the form of μ analysis (Morton and McAfoos, 1985), or by calculating the disk margins of the system (Seiler et al., 2020). These methods provide a deterministic solution to the robustness problem, but do not account for the additional complexity of nonlinear behaviour, which is inherent to any aerodynamic system.

Alternatively, a more stochastic methodology can be used in the form of the Monte Carlo approach (Ray and Stengel, 1993). Generally, this method is computationally expensive and risks missing a parameter variation combination that can make the system unstable. However, work by Postlethwaite et al. (2009) and Tempo and Dabenne (2004) applies the Chernoff Bound to calculate the lower bound for the number of samples which must be used to gain a given accuracy and confidence in a system's robustness. This proved extremely useful for the analysis conducted in Chapter 4.

3 Mathematical Modelling

Before a controller can be designed, a mathematical model of the system must be derived. This model must accurately describe the behaviour of the system dynamics within the expected operating conditions without being overly computationally expensive.

3.1 Frames of Reference

Two frames of reference are used here. The body frame, B, is fixed to the rocket during flight. It is a right-handed coordinate system with origin at the rocket's CG, and the x_B axis parallel to the rocket's longitudinal axis, pointing upwards towards the nose. The y_B and z_B axes are then orthogonal and lie on the rocket's cross section.

The global frame, G, is a right-handed coordinate system with its origin fixed to the ground at the location of the launch pad. The x_G axis points directly upwards, perpendicular to the ground and the y_G and z_G axes are orthogonal to it parallel to the ground. The flight is low-altitude and lasts less than a minute, and therefore the Earth's rotation has been neglected and the ground has been modelled as a flat plane.

At the time of ignition, the body and global frames are aligned, but do not remain so during flight. The rocket's roll, pitch and yaw angles, ϕ, θ, and ψ, are then defined as the Euler angles that compose the rotation, R, such that any vector, $\mathbf{a} \in \mathbb{R}^3$, is transformed from the global frame to the body frame, as in (3.1).

$$\mathbf{a}_B = \mathrm{R}(\phi, \theta, \psi)\, \mathbf{a}_G \tag{3.1}$$

3.2 Pitch and Yaw Moments

It has been assumed that there are three moments acting on the rocket's pitch and yaw axes during flight.

M_{corr}	Corrective moment induced by the lift acting on the rocket's passive fins.
M_{damp}	Damping moment induced by the drag on the airframe as it rotates.
M_{can}	Canard moment induced by the lift of the deflected canards.

3.2.1 Pitch / Yaw Corrective Moment

Providing that the rocket's CP is further aft than its CG, there will be a corrective moment acting to align the rocket with the incoming air flow. In the presence of a crosswind, this moment will reduce the rocket's angle of attack. Mandell et al. (1973) state that the pitch and yaw corrective moments, M_{corr} and N_{corr}, acting on the rocket are proportional to the angle of attack as in (3.2).

$$M_{corr} = C_1 \alpha \quad , \quad N_{corr} = C_1 \beta \tag{3.2}$$

Where C_1 is the corrective moment coefficient, given by (3.3) and derived by Mandell et al. (1973).

$$C_1 = \bar{q} A_{ref} C_{N_\alpha} \bar{X}_{CP} \tag{3.3}$$

Where $\bar{q}$ is the dynamic pressure of the airflow, $\bar{q} = \frac{1}{2}\rho v^2$, A_{ref} is the body tube's cross-sectional area, and $\bar{X}_{CP}$ is the moment arm between the CP and the CG: $\bar{X}_{CP} = X_{CP} - X_{CG}$. C_{N_α} is the rocket's normal force coefficient derivative with respect to angle of attack. The methods used to calculate this parameter were derived by Niskanen (2009) and Youds (2022) and are included in Appendix A.

3.2.2 Pitch / Yaw Damping Moment

Mandell et al. (1973) also derive the rocket's pitch and yaw damping moments, and as expected, these are proportional to the pitch rate, q, and yaw rate, r, respectively.

$$M_{damp} = C_2 q \quad , \quad N_{damp} = C_2 r \tag{3.4}$$

Where C_2 is the damping moment coefficient, derived by Mandell et al. (1973).

$$C_2 = \frac{\bar{q}}{v} A_{ref} \left[\sum C_{N_{\alpha_i}} \bar{X}_{CP_i}{}^2 \right] + \dot{m} \bar{X}_T^2 \tag{3.5}$$

Where $C_{N_{\alpha_i}}$ is the normal force coefficient derivative of the i^{th} fuselage component, (e.g., nose cone, body tube, or fins), and $\bar{X}_{CP_i}$ is the moment arm between the rocket's CG and the CP of the i^{th} component: $\bar{X}_{CP_i} = X_{CP_i} - X_{CG}$. The first term here represents the aerodynamic damping due to drag as the rocket rotates, and the second represents the jet damping.

Jet damping is an additional damping torque induced by the jet of exhaust gases leaving the engine. This fast-moving gas resists changes in rotational momentum and helps to keep the rocket flying straight. $\dot{m}$ is the mass flow rate of the exhaust gas, and $\bar{X}_T$ is the moment arm between the rocket's CG and the engine throat.

3.2.3 Pitch / Yaw Canard Moment

When the canards are deflected, the lift force they generate induces pitch and yaw moments on the rocket. Figure 5 in Appendix D shows the canard configuration.

Two canards on opposite sides of the rocket control pitch motion about the y_B axis. The canard moment, M_{can}, is equal to the distance between the rocket's CG and the CP of the canards multiplied by the horizontal component of the canard lift force. Drag can be

assumed to be negligible here since the canard $^{L}/_{D}$ ratio is approximately 120 (Daney de Marcillac, 2023). Therefore, the canard pitch moment is given by (3.6).

$$M_{can} = \bar{q}S\bar{X}_{CP_{can}}(C_{L_1}\cos x_1 + C_{L_2}\cos x_2) \tag{3.6}$$

The lift coefficient itself is proportional to angle of attack. The angle of attack on the canard depends on the rocket's angle of attack, α, and the canard deflection, x_i. The sign convention for the canard deflections is important here. Since the body frame origin lies at the CG, one canard lies on the y_B^+ axis – canard 1 – and the other on the y_B^- axis – canard 2. The deflections of these canards are x_1 and x_2 respectively.

A positive x_1 deflection generates a positive pitching moment, as per the righthand screw rule. The opposite is true for canard 2; a positive x_2 deflection results in a negative pitching moment. Therefore, if $x_1 = x_2$, there will be no pitching motion, only rolling motion. Consequently, the AoA on canard 1 is the difference between α and x_1, whereas for canard 2, it is the sum of α and x_2. Applying this to (3.6) gives (3.7).

$$C_{L_i} = C_{L_\alpha}\alpha_{can_i}$$

$$\Rightarrow M_{can} = \bar{q}SC_{L_\alpha}\bar{X}_{CP_{can}}[(\alpha - x_1)\cos x_1 + (\alpha + x_2)\cos x_2] \tag{3.7}$$

For simplicity of notation, the pitch moment derivative with respect to canard angle of attack can be defined as $M_\alpha = \bar{q}SC_{L_\alpha}\bar{X}_{CP_{can}}$. Applying this substitution to (3.7) gives (3.8).

$$M_{can} = M_\alpha[(\alpha - x_1)\cos x_1 + (\alpha + x_2)\cos x_2] \tag{3.8}$$

This is also true for the yaw canard moment, N_{can}.

$$N_{can} = N_\alpha[(\beta - y_1)\cos y_1 + (\beta + y_2)\cos y_2] \tag{3.9}$$

3.3 Roll Moments

Two moments act on the rocket's roll axis. Since the Pathfinder fins are mounted on bearings and can spin freely, it has been assumed that the only roll forcing moment is due to the canards.

L_{damp}	Damping moment induced by the drag on the airframe as it rotates.
L_{can}	Canard moment induced by the lift of the deflected canards.

3.3.1 Roll Damping Moment

Youds (2022) expands Niskanen's (2009) work to show that the roll damping moment is proportional to the rocket's roll rate, p, as in (3.16).

$$L_{damp} = C_{d_p}p \tag{3.10}$$

Where C_{d_p} is the roll damping coefficient with respect to roll rate (Youds, 2022).

$$C_{d_p} = \frac{\bar{q}}{v} A_{ref} d_{body} N C_{N_{\alpha_0}} \left(\sum c_i \xi_i^2 \Delta \xi_i \right) \tag{3.11}$$

Where d_{body} is the body tube diameter and $C_{N_{\alpha_0}}$ is the normal force coefficient of the fin's 2D aerofoil. The final sum term is constant for a specific fin planform shape and is given by Youds (2022) and Niskanen (2009).

3.3.2 Roll Canard Moment

The canard roll moment is defined by (3.12). Figure 6 in Appendix D shows the directions of these forces. Again, the drag on the canards has been neglected.

$$L_{can} = \bar{Y}_{CP_{can}} F_{x_1} - \bar{Y}_{CP_{can}} F_{x_2} + \bar{Z}_{CP_{can}} F_{y_1} - \bar{Z}_{CP_{can}} F_{y_2} \tag{3.12}$$

Where $\bar{Y}_{CP_{can}}$ and $\bar{Z}_{CP_{can}}$ are the moment arms between the CG and the CP of the canards in the y_B and z_B axes respectively. It is assumed that the CG lies on the body frame origin, and therefore $\bar{Y}_{CP_{can}} = Y_{CP_{can}}$ and $\bar{Z}_{CP_{can}} = Z_{CP_{can}}$. Moreover, the canards are placed symmetrically about the x axis, and thus $Y_{CP_{can}} = Z_{CP_{can}}$.

F_{x_1}, F_{x_2}, F_{y_1}, and F_{y_2} are the components of the lift forces acting in the $y_B - z_B$ plane. Since $F_i = \bar{q} S C_{L_\alpha} \alpha_{can_i} \cos x_i$, and using the angles of attack derived in Section 3.2.3, the total moment can be expressed in the form shown in (3.13).

$$L_{can} = L_\alpha [(\alpha - x_1)\cos x_1 - (\alpha + x_2)\cos x_2 + (\beta - y_1)\cos y_1 - (\beta - y_2)\cos y_2] \tag{3.13}$$

Where $L_\alpha = \bar{q} S C_{L_\alpha} Y_{CP_{can}} = \bar{q} S C_{L_\alpha} Z_{CP_{can}}$ is the derivative of the canard roll moment with respect to the angle of attack of the respective canard.

3.4 Equation of Motion Formulation

Euler's Rotational Equation of Motion relates the rocket's rotational accelerations, $\dot{\boldsymbol{\omega}}$, and rates, $\boldsymbol{\omega}$, to the moments acting on it during flight, as shown in (3.14).

$$\mathrm{J}\dot{\boldsymbol{\omega}} + \boldsymbol{\omega} \times (\mathrm{J}\boldsymbol{\omega}) = \mathbf{M} \tag{3.14}$$

Where J is the rocket's moment of inertia matrix. It can be assumed that the rocket is axisymmetric about the x_B axis, and therefore J is given by (3.15).

$$\mathrm{J} = \{J_R \quad J_L \quad J_L\}^T \cdot \mathrm{I}_3 \tag{3.15}$$

Where J_R and J_L are the rocket's radial and longitudinal mass moments of inertia respectively and I_n is the $n \times n$ identity matrix.

The resultant moment vector, $\mathbf{M}$, is given by (3.16).

$$\mathbf{M} = \begin{bmatrix} L_{can} - L_{damp} \\ M_{can} - M_{corr} - M_{damp} \\ N_{can} - N_{corr} - N_{damp} \end{bmatrix}$$

$$\Rightarrow \mathbf{M} = \begin{bmatrix} L_\alpha[(\alpha - x_1)\cos x_1 - (\alpha + x_2)\cos x_2 + (\beta - y_1)\cos y_1 - (\beta + y_2)\cos y_2] - C_{d_p}p \\ M_\alpha[(\alpha - x_1)\cos x_1 + (\alpha + x_2)\cos x_2] - C_1\alpha - C_2 q \\ N_\alpha[(\beta - y_1)\cos y_1 + (\beta + y_2)\cos y_2] - C_1\beta - C_2 r \end{bmatrix} \quad (3.16)$$

Equations (3.15) and (3.16) were substituted into (3.14) to give the rotational equations of motion for the rocket. The final equation has been omitted here for the sake of brevity.

3.5 Nonlinear Modelling

To run simulations of the rocket's motion and tune the controller, the nonlinear dynamics equation (3.14) was implemented in Simulink. Aerodynamic properties, such as the normal force coefficient derivatives and centres of pressure were calculated directly from Pathfinder's geometry using the equations discussed in Appendix A and the work of Youds (2022) and Niskanen (2009).

Mass properties, such as the mass moments of inertia, centre of gravity location, and exhaust gas mass flow rate were exported from OpenRocket. Lookup tables were implemented in Simulink to model the variation of these parameters throughout ascent.

The vertical velocity over time was also exported from OpenRocket and a range of profiles were tested to ensure the controller was not overly sensitive to velocity variations as this is something that was expected to be difficult to perfectly predict for the real flight.

The complexity of the modelling was increased over time. First, the system response was analysed at a single operating point, for example a constant velocity and altitude. This was used to ensure the system had adequate controllability before progressing.

A time variant model was then created, where the operating condition was itself a function of time, to better simulate a real flight. To start with, this model assumed a crosswind of constant speed and direction, acting only in the $y_G - z_G$ plane.

Later, this was improved, using Dryden's wind turbulence model in Simulink (MathWorks, n.d.). This model varied both the windspeed and direction based on the rocket's altitude and attitude. This was used to ensure the rocket could perform three axis control effectively and respond adequately to sudden gusts of wind. Full analysis of these results has not been included in the main body of the report due to space limitations, but graphs of the system performance for these models is in Appendix E.

4 Closed Loop Controller Design

4.1 States, Inputs, and Disturbances

To fly vertically, the controller works to minimise the rocket's roll, pitch, and yaw angles and rates. These six variables form the state vector, $\mathbf{x} \in \mathbb{R}^{\mathbf{6}}$, shown in (4.1), where ϕ, θ, and ψ are the roll, pitch and yaw angles respectively, and p, q, and r are their rates.

$$\mathbf{x} = \{\phi \quad \theta \quad \psi \quad p \quad q \quad r\}^T \tag{4.1}$$

These four angular canard deflections make up the input vector, $\mathbf{u} \in \mathbb{R}^{\mathbf{4}}$, shown in (4.2). The notation for the canard naming described in Chapter 3 is used again here.

$$\mathbf{u} = \{x_1 \quad x_2 \quad y_1 \quad y_2\}^T \tag{4.2}$$

As shown in Chapter 3, the angle of attack and sideslip angle, α and β, affect the lift generated by the canards, as well as the pitch and yaw corrective moments. Measuring these angles would require two angle of attack vanes as seen on aircraft, placed perpendicular to each other on the rocket's airframe (Gracey, 1958). Those used on aircraft are too large and heavy for use on Pathfinder, and therefore custom sensors would need to be designed, manufactured and tested, adding significant complexity.

Instead, α and β are modelled as disturbances and are not measured. The disturbance vector, $\mathbf{d} \in \mathbb{R}^{\mathbf{2}}$, is therefore of the form shown in (4.3).

$$\mathbf{d} = \{\alpha \quad \beta\}^T \tag{4.3}$$

4.2 State Space Formulation

The rocket's rotational equations derived in Chapter 3 are inherently nonlinear. A linear representation can be formed, known as the state space formulation, where the system dynamics are described by equation (4.4).

$$\begin{aligned} \dot{\mathbf{x}} &= \mathrm{A}\mathbf{x} + \mathrm{B}\mathbf{u} + \mathrm{E}\mathbf{d} \\ \mathbf{y} &= \mathrm{C}\mathbf{x} + \mathrm{D}\mathbf{u} + \mathrm{F}\mathbf{d} \end{aligned} \tag{4.4}$$

Where A, B, C, D, E, and F are matrices that relate the system states, inputs, and disturbances to the state derivative, $\dot{\mathbf{x}}$, and output, $\mathbf{y}$.

To obtain this formulation, the dynamics equations derived in Section 3.4 were rearranged in terms of the components of $\mathbf{x}$, $\mathbf{u}$, and $\mathbf{d}$. These equations were then linearised around the steady-state operating point $\bar{\mathbf{x}} = 0$, using the first-order Taylor series and small angle approximations. Full derivation of the state space equation is presented as Appendix B. The final state space representation is shown as (4.5).

$$\dot{\mathbf{x}} = \begin{bmatrix} 0 & 0 & 0 & 1 & 0 & 0 \\ 0 & 0 & 0 & 0 & 1 & 0 \\ 0 & 0 & 0 & 0 & 0 & 1 \\ 0 & 0 & 0 & -\frac{C_{d_p}}{J_R} & 0 & 0 \\ 0 & 0 & 0 & 0 & -\frac{C_2}{J_L} & 0 \\ 0 & 0 & 0 & 0 & 0 & -\frac{C_2}{J_L} \end{bmatrix} \mathbf{x} + \begin{bmatrix} 0 & 0 & 0 & 0 \\ 0 & 0 & 0 & 0 \\ 0 & 0 & 0 & 0 \\ -\frac{L_\alpha}{J_R} & -\frac{L_\alpha}{J_R} & -\frac{L_\alpha}{J_R} & -\frac{L_\alpha}{J_R} \\ -\frac{M_\alpha}{J_L} & +\frac{M_\alpha}{J_L} & 0 & 0 \\ 0 & 0 & -\frac{N_\alpha}{J_L} & +\frac{N_\alpha}{J_L} \end{bmatrix} \mathbf{u} + \begin{bmatrix} 0 & 0 \\ 0 & 0 \\ 0 & 0 \\ 0 & 0 \\ 2\frac{M_\alpha}{J_L} - \frac{C_1}{J_L} & 0 \\ 0 & 2\frac{N_\alpha}{J_L} - \frac{C_1}{J_L} \end{bmatrix} \mathbf{d} \quad (4.5)$$

$$\mathbf{y} = \mathrm{I}_6 \mathbf{x}$$

4.3 LQR Design

Once the state space representation was formed, the LQR controller was tuned. Figure 1 shows the layout of the closed loop control system.

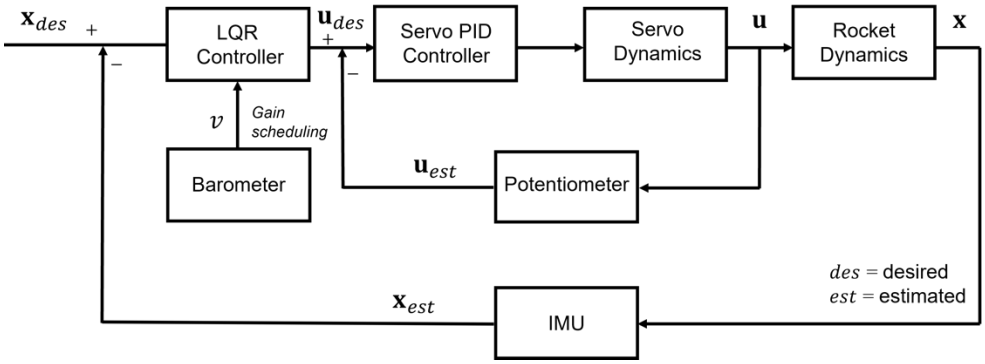

Figure 1 - Closed loop control diagram of the Aptos control system.

The LQR controller acts as a 4×6 pure gain matrix, K, applied to the state error in order to derive the desired control inputs, $\mathbf{u}$. These gains are calculated by minimising the cost function (4.6), where $\mathbf{u} = -\mathrm{K}\,\mathbf{x}$ and Q and R are the state-cost and input-cost weighted matrices (Yang, 2012; Okyere et al., 2019).

$$J = \int_0^\infty \left(\mathbf{x}^{\mathrm{T}}\mathrm{Q}\mathbf{x} + \mathbf{u}^{\mathrm{T}}\mathrm{R}\mathbf{u}\right) dt \quad (4.6)$$

From inspection, this is an energy minimisation problem, where $\mathbf{x}^{\mathrm{T}}\mathrm{Q}\mathbf{x}$ represents the energy of the rocket due to its current state, and $\mathbf{u}^{\mathrm{T}}\mathrm{R}\mathbf{u}$ represents the energy associated with the actuation of the inputs.

In practice, to tune the controller, the MATLAB `lqr(A, B, Q, R)` function was used, where `A` and `B` represent the state space matrices from (4.5). The Q and R matrices are varied to achieve the desired performance. Since each canard is actuated by an identical servomotor, the cost was considered equal across all inputs and the input-cost weighted matrix was of the form shown in (4.6).

$$\mathrm{R} = r \cdot \mathrm{I}_4 \tag{4.6}$$

Where r is the actuator penalisation weight.

This was not the case for the state-cost weighted matrix, where individual weights were used to prioritise the reduction of some state errors more than others, as in (4.7).

$$\mathrm{Q} = \{q_\phi \quad q_\theta \quad q_\psi \quad q_p \quad q_q \quad q_r\}^T \cdot \mathrm{I}_6 \tag{4.7}$$

Where q_i are the weightings for each state.

For the first few flight tests, a priority was to ensure that the canard motion was as smooth as possible, avoiding sudden changes in deflection. This helps prevent the canards from undergoing dynamic stall and other nonlinear aerodynamic effects.

To achieve this, minimising the pitch and yaw angles was prioritised over minimising the pitch and yaw rates. Thus, $q_\theta > q_q$ and $q_\psi > q_r$. As a result, the response was slightly slower acting and less damped, however the canard deflections were smoother.

During flight, minimising roll rate is significantly more important than roll angle. If the rocket begins to spin at a fast rate, a small pitch or yaw perturbation will lead to a significant gyroscopic precession known as coning (Youds, 2022). Pitch and yaw controllability will be significantly reduced to the point that instability could occur.

When the rocket rolls, it's important that the controller reduces the roll rate, but does not attempt to return the rocket to its original roll angle. To this end, the ideal roll angle weighting, q_ϕ, is zero. However, one condition of the LQR controller is that both the Q and R matrices must be positive definite (Yang, 2012) and therefore a very small value is used such that $q_p \gg q_\phi$.

The specific values of the q and r weighting factors were determined through trial-and-error until the Simulink simulations indicated that the system met the performance requirements. Bryson's Rule (Okyere et al., 2019) was investigated as a method to achieve this algorithmically, although the gains this produced were very high and it was later found that comparable performance could be achieved with significantly lower gains. The final weightings are shown in (4.8) and (4.9).

$$\mathrm{Q} = \{1 \times 10^{-9} \quad 4 \quad 4 \quad 4 \quad 1 \quad 1\}^T \cdot \mathrm{I}_6 \tag{4.8}$$

$$\mathrm{R} = 5 \cdot \mathrm{I}_4 \tag{4.9}$$

4.4 Gain Scheduling

Every aerodynamic property of the system varies with velocity, and most are proportional to the velocity squared. Intuitively, the controller will require significantly less actuator effort when the rocket is flying at higher speeds than it does when at low speeds.

Gain scheduling was implemented to ensure that the controller could account for these velocity changes as the rocket accelerates. Optimum gain-sets were calculated at different velocities from 30 m/s up to 150 m/s (about 1.5x the expected maximum speed). The onboard flight computer then hands off between gain-sets as the differentiated barometer data indicates that the vertical velocity has changed. Gain scheduling significantly improved performance across the full velocity profile with very little memory cost on the flight computers.

4.5 Servomotor Position Control

The analysis up to this point has assumed that the LQR controller can command a certain canard deflection, and this deflection is achieved instantly. In reality, both time delay and position error are present in the servomotors, and this affects the system's performance.

The Herkulex DRS-0101 motors used in the Aptos module were smart servos and featured an in-built potentiometer and PID controller for position control. The PID gains could be written directly to the servos' RAM, meaning that different combinations could be tested quickly and easily.

From requirements APT-REQ-1-5-1 and APT-REQ-1-5-6, the servomotors must respond to a 10° step input with a settling time less than 0.1 s and an accuracy of $\pm 0.5°$ with no overshoot outside of these bounds. In addition, a pointing accuracy of $1 \pm 0.1°$ is needed to ensure the servos have the fine control required for flight (APT-REQ-1-5-5).

This was achieved through a trial-and-error testing process. One of the servos was connected to a computer via an Arduino Uno development board and a step input was commanded. The angular position of the servo was read from its potentiometer, and the PID gains were iteratively tuned until performance met the requirements.

Figure 2 shows the response to both a 1° and 10° step input. The PID gains used are displayed in Table 1.

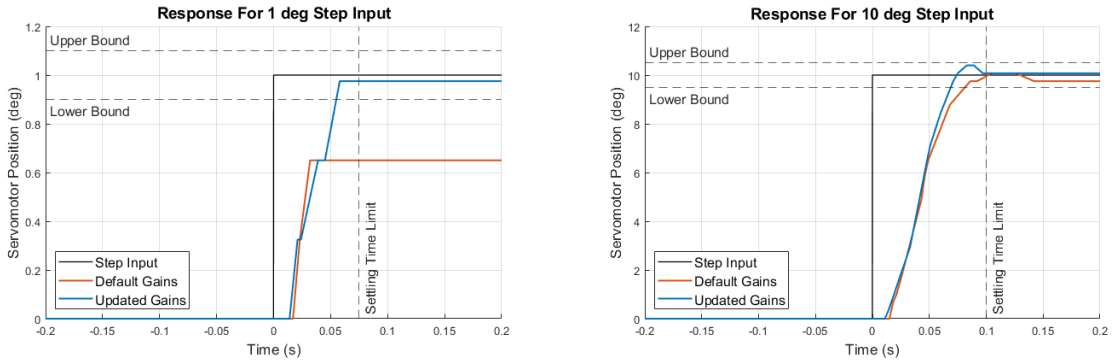

Figure 2 - Servomotor position step response graphs with the default and updated PID gain sets for steps of 1° and 10°.

Table 1 - PID gains used for the servomotor position controller.

	K_p	K_i	K_d
Default	440	0	8000
Updated	550	1000	9000

The default gains provided a good response for the 10° step, however the performance for the 1° step was poor. The servomotors operate in increments of 0.325°, and the gains were not high enough to overcome the internal friction needed to step through the final increment, thus the shaft gets stuck at 0.65°. Similar plateaus can be seen in the updated gain response, however the higher K_p and K_i gains forced the controller to overcome the frictional force.

The updated response for the 10° step was very good. There was a small amount of overshoot, but this was within acceptable bounds. Increasing the K_d gain further reduced this overshoot but slowed the response for the 1° step too much.

Using the MATLAB System Identification App and the step data shown in Figure 2, a transfer function was fit, which represented the servomotor position control dynamics. This was used in Simulink to model the delay and position error associated with actuating the canards.

4.6 Robustness Analysis

Requirement APT-REQ-1-1-1 states that the controller must be robust to expected deviations from the geometry of the Pathfinder rocket with 95% accuracy and confidence. Specifically, the nominal values and expected variability of each of these parameters are provided in Appendix C.

The Chernoff Bound can be used to calculate the number of samples needed to gain the required accuracy and confidence, as in (4.8) (Postlethwaite et al., 2009).

$$N \geq \frac{\log(2/\delta)}{2\epsilon^2} \tag{4.8}$$

Applying $\epsilon = \delta = 0.05$ gives a minimum sample number of 737.8. In total, 740 simulations were run. Figure 3 shows how the system is robust both in terms of performance and stability across the entire expected parameter variation. This model assumes a constant windspeed of 5 m/s acting only in the z_G^+ direction.

This is expected as the LQR is an inherently robust controller, however it is impressive that the system can handle up to $\pm$50% variation in the canard C_{L_α} value. This fact prevented the need for any high fidelity aerodynamic modelling of the canards.

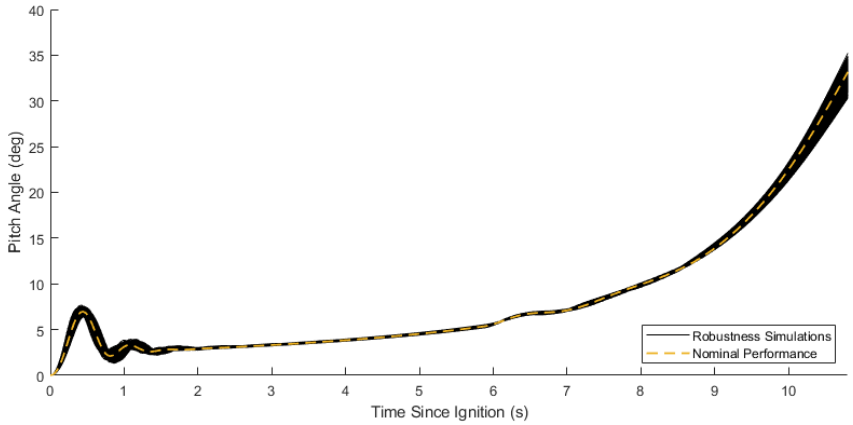

Figure 3 - Results from the control system robustness analysis.

4.7 Controller Performance

Figure 4 displays how the system handles a 5 m/s constant crosswind. In this simulation, the wind vector acted solely in the z_G^+ direction and therefore induced pitch motion only. For comparison, the free response without active control enabled is also plotted on Figure 4.

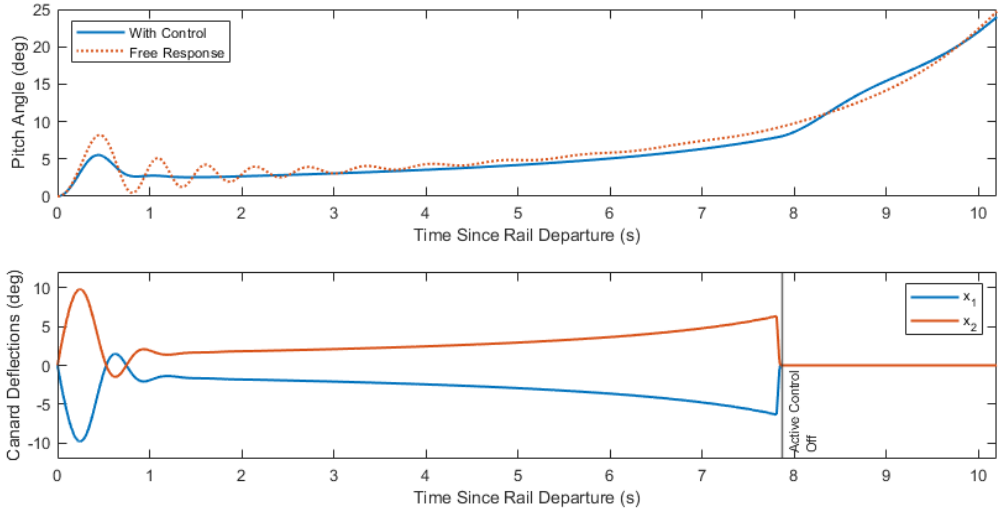

Figure 4 - System performance with 5 m/s constant crosswind.

The control algorithm was set to only activate whilst the vertical velocity, $v \geq 30$ m/s. This prevented it from activating whilst the rocket was still on the launch rail and minimises actuator energy cost towards apogee when the velocity is too low for the rocket to be controllable.

The Aptos system reduced the peak pitch angle by about 2.7° and significantly damped the oscillations following rail departure. The steady state pitch angle during ascent is very similar for both cases, as is the increase in pitch as the rocket decelerates towards apogee. This system provides a good first proof-of-concept, and performance can be significantly improved by reducing the input-cost weighting matrix, R.

5 Conclusion

5.1 Achievements and Impact

This project aimed to develop the active control algorithm for a canard-controlled sounding rocket stability augmentation system. First, the work of Mandell et al. (1973), Niskanen (2009), and Youds (2022) was expanded to derive a three degree of freedom dynamic model of a canard-controlled sounding rocket. This model was linearised using first order Taylor series techniques and small angle approximations, and an LQR controller was tuned to minimise the rocket's attitude and attitude rates throughout ascent. A separate PID controller was tuned to improve the response of the servomotors that control the canards, and system identification techniques were used to model the actuator's behaviour in Simulink. Finally, the system's performance was verified and its robustness was analysed using stochastic methods derived by Postlethwaite et al. (2009) and Tempo and Dabenne (2004).

The performance of the LQR controller in simulations indicated that it met the requirements set out in the project's contract performance plan. Moreover, due to the controller's inherent robustness, it has been proven to handle significant variations in rocket and canard geometry with almost no cost to performance or stability. Specifically, this was verified with both an accuracy and confidence of 95%.

Significant progress has been made towards developing a fully functional, modular canard control system. Although full flight testing has not yet been possible, the two data acquisition flights conducted throughout this project were highly successful. The performance of the control algorithm during both flights was nominal and indicates a high likelihood of success in the future. More discussion on the control algorithm's performance during these flights is included in Youds et al. (2023).

5.2 Future Work

More flight tests are already planned for the remainder of 2023, specifically aiming to fly several times with the active control system enabled. Future work will make use of the existing datasets to improve confidence in the system and increase performance further. For example, adaptive control techniques could be employed, using real flight data to tune the next iteration of the Aptos control algorithm.

It is also recommended that hardware-in-the-loop testing is conducted using flight data as further improvements in performance can likely be found in the optimisation of the embedded software running the algorithm.

6 References

Braswell, V., Arcenaux, H., Strutzenberg, H., Taylor, R. and Lineberry, D.M. 2017. UAH Student Launch Rocket Project: Roll Control of a Sounding Rocket Through Aerodynamic Surfaces *In*: *53rd AIAA/SAE/ASEE Joint Propulsion Conference* [Online]. Atlanta, GA: American Institute of Aeronautics and Astronautics. [Accessed 2 December 2021]. Available from: https://arc.aiaa.org/doi/10.2514/6.2017-4840.

Choi, H.-D. and Bang, H. 2000. An adaptive control approach to the attitude control of a flexible rocket. *Control Engineering Practice*. **8**(9), pp.1003–1010.

Daney de Marcillac, J. 2023. *Design and Aerodynamic Analysis of a Canard-Controlled Sounding Rocket*. Leeds, UK: University of Leeds.

Gracey, W. 1958. Summary of Methods of Measuring Angle of Attack on Aircraft. Available from: https://ntrs.nasa.gov/api/citations/19930085167/downloads/19930085167.pdf.

Guo, Q., Song, W., Gao, M. and Fang, D. 2016. Advanced Guidance Law Design for Trajectory-Corrected Rockets with Canards under Single Channel Control.

James Barrowman 1967. *The Practical Calculation of the Aerodynamic Characteristics of Slender Finned Vehicles*.[Online] Washington D.C.: The Catholic University of America. [Accessed 13 December 2021]. Available from: https://ntrs.nasa.gov/api/citations/20010047838/downloads/20010047838.pdf.

Lorenz, S. and Bierig, A. 2013. Robustness Analysis Related to the Control Design of the SHEFEX-II Hypersonic Canard Control Experiment *In*: *AIAA Guidance, Navigation, and Control (GNC) Conference* [Online]. Boston, MA: American Institute of Aeronautics and Astronautics. [Accessed 1 May 2023]. Available from: https://arc.aiaa.org/doi/10.2514/6.2013-4857.

Mandell, G.K., Caporaso, G.J. and Bengen, W.P. 1973. *Topics in advanced model rocketry*. Cambridge, Mass: MIT Press.

MathWorks n.d. Dryden Wind Turbulence Model (Continuous). *MATLAB and Simulink Documentation*. [Online]. Available from: https://uk.mathworks.com/help/aeroblks/drydenwindturbulencemodelcontinuous.html.

Morton, B.G. and McAfoos, R.M. 1985. A Mu-Test for Robustness Analysis of a Real-Parameter Variation Problem *In*: *1985 American Control Conference* [Online]. Boston, MA, pp.135–138. Available from: https://ieeexplore.ieee.org/abstract/document/4788593.

Mracek, C. and Ridgely, D. 2006. Optimal Control Solution for Dual (Tail and Canard) Controlled Missiles *In*: *AIAA Guidance, Navigation, and Control Conference and Exhibit* [Online]. Keystone, Colorado: American Institute of Aeronautics and Astronautics. [Accessed 1 May 2023]. Available from: https://arc.aiaa.org/doi/10.2514/6.2006-6569.

Narkiewicz, J., Sochacki, M. and Zakrzewski, B. 2020. Generic Model of a Satellite Attitude Control System. *International Journal of Aerospace Engineering*. **2020**, pp.1–17.

NAROM Andøya Space Centre 2018. Aerodynamics and forces acting on the rocket. *NAROM Student Rocket Pre-Study*. [Online]. [Accessed 21 June 2021]. Available from: https://www.narom.no/undervisningsressurser/sarepta/rocket-theory/rocket-dynamics-2/4-1aerodynamics-and-forces-acting-on-the-rocket/.

Niskanen, S. 2009. *Development of an Open Source model rocket simulation software*.[Online] Helsinki: Helsinki University of Technology. [Accessed 28 July 2021]. Available from: https://openrocket.info/documentation.html.

Okyere, E., Bousbaine, A., Poyi, G.T., Joseph, A.K. and Andrade, J.M. 2019. LQR controller design for quad-rotor helicopters. *The Journal of Engineering*. **2019**(17), pp.4003–4007.

Postlethwaite, I., Kim, J. and Bates, D.G. 2009. A geometrical formulation of the μ-lower bound problem. *IET Control Theory & Applications*. **3**(4), pp.465–472.

Ray, L.R. and Stengel, R.F. 1993. A monte carlo approach to the analysis of control system robustness. *Automatica*. **29**(1), pp.229–236.

Seaberg, E. and Smith, E. 1951. Theoretical Investigation Of An Automatic Control System With Primary Sensitivity To Normal Accelerations As Used To Control A Supersonic Canard Missile Configuration.

Seiler, P., Packard, A. and Gahinet, P. 2020. An Introduction to Disk Margins.

Tempo, R. and Dabbene, F. 2004. An Overview on Randomized Algorithms for Analysis and Control of Uncertain Systems. Available from: https://apps.dtic.mil/sti/pdfs/ADA431583.pdf.

Ujjin, R., Chaikiandee, S. and Ngaongam, C. 2021. Low Altitude Local Rocket Aerodynamics Analysis and Experimental Testing *In*: basel, Switzerland: MDPI.

UKRA 2021. UK Rocketry Altitude Records | UKRA - United Kingdom Rocketry Association. [Accessed 3 November 2022]. Available from: http://ukra.org.uk/records/allclass.

Uselton, J. 1971. *Results of an Air Force Advanced Tactical Rocket Development Program* [Online]. [Accessed 1 May 2023]. Available from: https://apps.dtic.mil/sti/citations/AD0885643.

Vigneswaran, R. and Kp, S. 2019. *An Insight into the Dynamics and State Space Modelling of a 3-D Quadrotor*.

Yang, Y. 2012. Analytic LQR Design for Spacecraft Control System Based on Quaternion Model. *Journal of Aerospace Engineering*. **25**(3), pp.448–453.

Youds, T. 2022. Feasibility Analysis of a Reaction Wheel System for Sounding Rocket Roll Control.

Youds, T., Cradock, B., Devlin, L., Whittaker, J. and Daney de Marcillac, J. 2023. *Development of a Canard Controlled Active Stability System for a Sounding Rocket*. Leeds, UK: University of Leeds.

Appendix A – Supporting Formulae Derivation

This appendix has been lifted from Youds (2022) to support the derivation of the aerodynamic equations in Chapter 3.

Normal Force Coefficient

The forces acting on the rocket in the body frame of reference can be divided into those acting axially, i.e. along the x_B axis, and those acting radially, i.e. normal to the x_B axis.

The axial force components generally act through the rocket's CG, or at such a small offset that the resulting moments are much smaller than those generated by the normal force components. Only the rocket's rotational motion is of interest here and therefore the axial force components have been omitted from the model.

Assuming that the thrust from the motor acts directly along the x_B axis, the only normal force components acting on the rocket are from gravity, when flying at a non-zero pitch/yaw angle, and from aerodynamic lift and drag. Rockets fly at very small pitch and yaw angles, and therefore the gravity component can generally be neglected with little effect on the model's accuracy.

Niskanen (2009) proposes that this aerodynamic normal force, N, can be calculated by (A.1)

$$N = \frac{1}{2}\rho v^2 A_{ref} C_N \qquad (A.1)$$

Where ρ is the air density, v is the freestream air velocity, A_{ref} is a reference area, generally taken as the cross-sectional area of the rocket's fuselage, and C_N is the rocket's normal force coefficient.

This normal force is generated by the culmination of lift and drag generated when the freestream air flows around the rocket body. Generally, rockets have axisymmetric body components and fins with symmetrical aerofoils, and therefore generate no normal force when flying at zero angle of attack, $\alpha = 0$. However, for $\alpha > 0$, these forces can be significant and greatly affect the rotational motion of the rocket.

The variation of the normal force with angle of attack is described by C_{N_α}, the angle of attack derivative of the normal force coefficient – referred to as the normal force coefficient derivative from here on. Niskanen (2009), extending on the work of Barrowman (1967), states that the normal force coefficient varies linearly with angle of attack, for small values of α. This relationship is given in equation (A.2).

$$C_{N_\alpha} = \frac{\partial C_N}{\partial \alpha}|_{\alpha=0} \Rightarrow \quad C_N \approx C_{N_\alpha}\alpha \tag{A.2}$$

Niskanen (2009) provides methods for calculating the normal force coefficient derivative, C_{N_α}, based on the rocket's geometry and flight conditions, such as speed and angle of attack. C_{N_α} is calculated for each section of the rocket: nose, body and fins, and then summed to find the value for the full vehicle.

Calculating C_{N_α} for Axisymmetric Body Components

The nosecone and fuselage can be treated as two separate axisymmetric body components. Niskanen (2009) derives equation (A.3) for finding C_{N_α} of such components. This approximation is very similar to that derived by Barrowman (1967) but applies to a larger range of α by not assuming that $\sin\alpha = \alpha$. The second term in equation (A.3) is used to include the effect of body lift when flying at significant angles of attack.

$$C_{N_\alpha} = \frac{2}{A_{ref}}[A(l) - A(0)]\frac{\sin\alpha}{\alpha} + K\frac{A_{plan}}{A_{ref}}\frac{\sin^2\alpha}{\alpha} \tag{A.3}$$

Where $A(x)$ is the area at position x along the component's length, A_{plan} is the planform area of the body component, and $K \approx 1.1$ is a correction factor. Care must be taken when using this equation to avoid singularities at $\alpha = 0$. This is achieved by implementing limit conditions, as shown by equations (A.4).

$$\lim_{\alpha\to 0}\frac{\sin\alpha}{\alpha} = 1 \quad , \quad \lim_{\alpha\to 0}\frac{\sin^2\alpha}{\alpha} = 0 \tag{A.4}$$

Calculating C_{N_α} for Fins

Making use of Diederich's semi-empirical method, Barrowman (1967) derived equation (A.5) to calculate the normal force coefficient derivative for a single fin (Niskanen, 2009).

$$\left(C_{N_\alpha}\right)_1 = \frac{C_{N_{\alpha_0}} F_D\left(\frac{A_{fin}}{A_{ref}}\right)\cos\Gamma_c}{2 + F_D\sqrt{1+\frac{4}{F_D^2}}} \tag{A.5}$$

Where $C_{N_{\alpha_0}}$ is the normal force coefficient derivative of the 2D aerofoil, F_D is Diedrich's planform correlation parameter, A_{fin} is the planform area of one fin, and Γ_c is the midchord sweep angle.

The 2D aerofoil normal force coefficient derivative, $C_{N_{\alpha_0}}$, can be found based on thin aerofoil theory, as in equation (A.6) (Niskanen, 2009).

$$C_{N_{\alpha_0}} = \frac{2\pi}{\sqrt{1-M^2}} \tag{A.6}$$

Where M is the local Mach number. Gryphon I-C remains subsonic during flight, therefore $M < 1$.

Diederich provides equation (A.7) for calculating F_D.

$$F_D = \frac{AR}{\frac{1}{2\pi} C_{N_{\alpha_0}} \cos \Gamma_c} \tag{A.7}$$

Where AR is the fin aspect ratio. $AR = 2s^2/A_{fin}$, where s is the fin semi-span, can be substituted into equation (A.7). Then substituting (A.7) and (A.6) into (A.5) gives an equation for the normal force coefficient derivative for a single fin as a function of the geometry and the Mach number. This is presented as equation (A.8).

$$\left(C_{N_\alpha}\right)_1 = \frac{2\pi \frac{s^2}{A_{ref}}}{1 + \sqrt{1 + \left(\frac{s^2\sqrt{1-M^2}}{A_{fin} \cos \Gamma_c}\right)^2}} \tag{A.8}$$

Niskanen (2009) then shows that the normal force coefficient derivative for k fins is found by multiplying the value for one fin by the sum of $\sin^2 \Lambda_i$ where Λ_i is the dihedral angle of the fin relative to the incoming lateral airflow.

$$\sum_{i=1}^{k} \left(C_{N_\alpha}\right)_k = \left(C_{N_\alpha}\right)_1 \sum_{i=1}^{k} \sin^2 \Lambda_i \tag{A.9}$$

Fortunately, for rockets with three or more equally spaced fins, the sum term reduces to $k/2$. Thus, for Pathfinder, with four fins, equation (A.10) applies.

$$\left(C_{N_\alpha}\right)_4 = 2\left(C_{N_\alpha}\right)_1 \tag{A.10}$$

Finally, a correction term, $K_{T(B)}$ is applied to account for fin-body interference, defined by equation (A.11).

$$K_{T(B)} = 1 + \frac{r_t}{s + r_t} \tag{A.11}$$

Where r_t is the body radius at the fin position. Therefore, the final normal force coefficient derivative for Pathfinder's four fins is given by equation (A.12), where $\left(C_{N_\alpha}\right)_1$ is given by equation (3.9).

$$C_{N_{\alpha_{fins}}} = 2\left(C_{N_\alpha}\right)_1 \left(1 + \frac{r_t}{s + r_t}\right) \tag{A.12}$$

CP for Body Components

The centre of pressure of axially symmetric body components can be readily computed by equation (A.13) (Niskanen, 2009).

$$X_{CP} = \frac{l\,A(l) - V}{A(l) - A(0)} \tag{A.13}$$

Where V is the volume of the component.

CP for Fins

The fin centre of pressure location can be obtained from an empirical equation originally derived by Barrowman (1967).

$$X_{CP} = \frac{X_t}{3}\frac{C_r + 2C_t}{C_r + C_t} + \frac{1}{6}\frac{C_r^2 + C_t^2 + C_r C_t}{C_r + C_t} \tag{A.14}$$

Where $X_t = C_r - C_t$. This is measured from the leading edge so must be corrected to be measured from the nose cone tip before being incorporated into finding the full rocket CP.

Full Rocket CP

The full rocket centre of pressure is then found from the CP locations of each of the individual components along with their respective C_{N_α} values, as in equation (A.15)

$$X_{CP} = \frac{\sum_{i=1}^{n} X_{CP_i}\left(C_{N_\alpha}\right)_i}{\sum_{i=1}^{n}\left(C_{N_\alpha}\right)_i} \tag{A.15}$$

Appendix B – Linearisation

This appendix contains the mathematical derivation of the linearised dynamic equations referenced in Chapter 4.

Roll

The roll dynamic equation is given by (B.1).

$$J_R\dot{p} = L_\alpha[(\alpha - x_1)\cos x_1 - (\alpha + x_2)\cos x_2 + (\beta - y_1)\cos y_1 - (\beta + y_2)\cos y_2] - C_{d_p}p \qquad (B.1)$$

Expanding the brackets gives (B.2).

$$\begin{aligned} J_R\dot{p} = {} & +L_\alpha\alpha\cos x_1 \\ & -L_\alpha x_1\cos x_1 \\ & -L_\alpha\alpha\cos x_2 \\ & -L_\alpha x_2\cos x_2 \\ & +L_\alpha\beta\cos y_1 \\ & -L_\alpha y_1\cos y_1 \\ & -L_\alpha\beta\cos y_2 \\ & -L_\alpha y_2\cos y_2 \\ & -C_{d_p}p \end{aligned} \qquad (B.2)$$

The canard deflections are limited at $\pm$10° and therefore it can be assumed that $\cos x_1 = \cos x_2 = \cos y_1 = \cos y_2 = 1$, with only 1.5% error. Applying this assumption to (B.2), collecting like terms and dividing through by J_R gives (B.3), the linearised roll equation.

$$\dot{p} = -\frac{L_\alpha}{J_R}x_1 - \frac{L_\alpha}{J_R}x_2 - \frac{L_\alpha}{J_R}y_1 - \frac{L_\alpha}{J_R}y_2 - \frac{C_{d_p}}{J_R}p \qquad (B.3)$$

Pitch

The pitch dynamic equation is given by (B.4).

$$J_L\dot{q} + (J_R - J_L)pr = M_\alpha[(\alpha - x_1)\cos x_1 + (\alpha + x_2)\cos x_2] - C_1\alpha - C_2 q \qquad (B.4)$$

Rearranging and expanding the brackets gives (B.5).

$$
\begin{aligned}
J_R\dot{q} = &+M_\alpha \alpha \cos x_1 \\
&-M_\alpha x_1 \cos x_1 \\
&+M_\alpha \alpha \cos x_2 \\
&+M_\alpha x_2 \cos x_2 \\
&-C_1 \alpha \\
&-C_2 q \\
&-(J_R - J_L)pr
\end{aligned} \qquad (B.5)
$$

The final term is not yet linear as it contains the product of two variables. Taylor series linearisation can be applied to the final term, as in (B.6).

$$f(p,r) = -(J_R - J_L)pr$$

$$\Rightarrow f(p,r) \approx f(\bar{p},\bar{r}) + \frac{df}{dp}|_{p=\bar{p}}\,(p-\bar{p}) + \frac{df}{dr}|_{r=\bar{r}}\,(r-\bar{r}) \qquad (B.6)$$

$\bar{p}$ and $\bar{r}$ are steady state values, such that $\dot{p} = 0$ when evaluated at $p = \bar{p}$ and $r = \bar{r}$. It therefore follows that $f(\bar{p},\bar{r}) = 0$. Applying this simplification and substituting in deviation variables, defined by (B.7), forms equation (B.8).

$$
\begin{aligned}
p' &= p - \bar{p} \\
r' &= r - \bar{r}
\end{aligned} \qquad (B.7)
$$

$$\Rightarrow f(p,r) \approx -(J_R - J_L)\bar{r}\,p' - (J_R - J_L)\bar{p}\,r' \qquad (B.8)$$

There is an equilibrium in the system when all states in the state vector, $\mathbf{x}$, equal zero. Therefore $\bar{p} = \bar{r} = 0$ and consequently $f(p,r) = 0$.

Substituting this back into (B.6), applying the small angle approximation to the cosines in the first four terms, and dividing through by J_L gives (B.9), the linearised pitch motion equation.

$$\dot{q} = -\frac{M_\alpha}{J_L}x_1 + \frac{M_\alpha}{J_L}x_2 + \left(2\frac{M_\alpha}{J_L} - \frac{C_1}{J_L}\right)\alpha - \frac{C_2}{J_L}q \qquad (B.9)$$

Yaw

The nonlinear yaw dynamic equation is given by (B.10).

$$J_L\dot{r} + (J_L - J_R)pq = N_\alpha[(\beta - y_1)\cos y_1 + (\beta + y_2)\cos y_2] - C_1\beta - C_2 r \qquad (B.10)$$

The same process used to linearise the pitch equation was used for the yaw equation in (B.10). This gives (B.11), the linearised yaw motion equation.

$$\dot{r} = -\frac{N_\alpha}{J_L}y_1 + \frac{N_\alpha}{J_L}y_2 + \left(2\frac{N_\alpha}{J_L} - \frac{C_1}{J_L}\right)\beta - \frac{C_2}{J_L}r \qquad (B.11)$$

State Space Formulation

Equations (B.3), (B.9), and (B.11) provide a linear approximation of the rotational motion of the rocket in terms of the states, $\mathbf{x}$, inputs, $\mathbf{u}$, and disturbances, $\mathbf{d}$. This linear system of equations can be written as matrices in state space form, as in (B.12).

$$\begin{Bmatrix} \dot{p} \\ \dot{q} \\ \dot{r} \\ \dot{\dot{p}} \\ \dot{\dot{q}} \\ \dot{\dot{r}} \end{Bmatrix} = \begin{bmatrix} 0 & 0 & 0 & 1 & 0 & 0 \\ 0 & 0 & 0 & 0 & 1 & 0 \\ 0 & 0 & 0 & 0 & 0 & 1 \\ 0 & 0 & 0 & -\frac{C_{d_p}}{J_R} & 0 & 0 \\ 0 & 0 & 0 & 0 & -\frac{C_2}{J_L} & 0 \\ 0 & 0 & 0 & 0 & 0 & -\frac{C_2}{J_L} \end{bmatrix} \begin{Bmatrix} \phi \\ \theta \\ \psi \\ p \\ q \\ r \end{Bmatrix} + \begin{bmatrix} 0 & 0 & 0 & 0 \\ 0 & 0 & 0 & 0 \\ 0 & 0 & 0 & 0 \\ -\frac{L_\alpha}{J_R} & -\frac{L_\alpha}{J_R} & -\frac{L_\alpha}{J_R} & -\frac{L_\alpha}{J_R} \\ -\frac{M_\alpha}{J_L} & +\frac{M_\alpha}{J_L} & 0 & 0 \\ 0 & 0 & -\frac{N_\alpha}{J_L} & +\frac{N_\alpha}{J_L} \end{bmatrix} \begin{Bmatrix} x_1 \\ x_2 \\ y_1 \\ y_2 \end{Bmatrix} + \begin{bmatrix} 0 & 0 \\ 0 & 0 \\ 0 & 0 \\ 0 & 0 \\ 2\frac{M_\alpha}{J_L} - \frac{C_1}{J_L} & 0 \\ 0 & 2\frac{N_\alpha}{J_L} - \frac{C_1}{J_L} \end{bmatrix} \begin{Bmatrix} \alpha \\ \beta \end{Bmatrix} \quad (B.12)$$

Appendix C – Expected Parameter Variations

Table 2 displays the expected variations of parameters within the nonlinear model. These were generally obtained from taking the worst-case tolerance stack-up from the component's respective manufacturing processes. A very conservative approach was taken for aerodynamic components, especially those manufactured by hand, such as the rear fins.

The $\pm$50% variation on the canard lift coefficient derivative is to account for the inaccuracy of the aerodynamic simulations.

Table 2 - Parameter variations used for the robustness analysis of the control system.

Parameter		Nominal Value	Variation	Units
Radial moment of inertia	J_R	*	$\pm$ 20%	kg m^2
Longitudinal moment of inertia	J_L	*	$\pm$ 20%	kg m^2
Rocket body diameter	d_{body}	0.103	$\pm$ 0.003	m
Nose cone length	l_{nose}	0.507	$\pm$ 0.010	m
Rocket body length	l_{body}	1.563	$\pm$ 0.010	m
Fin semi-span	ss_{fin}	0.14	$\pm$ 0.002	m
Fin root chord length	$c_{r_{fin}}$	0.12	$\pm$ 0.002	m
Fin tip chord length	$c_{t_{fin}}$	0.065	$\pm$ 0.002	m
Rocket CG location	X_{CG}	1.32	$\pm$ 0.050	m
Canard CP location (x)	$X_{CP_{can}}$	0.589	$\pm$ 0.010	m
Canard CP location (y)	$Y_{CP_{can}}$	0.0865	$\pm$ 0.005	m
Canard CP location (z)	$Z_{CP_{can}}$	0.0865	$\pm$ 0.005	m
Canard semi-span	ss_{can}	0.07	$\pm$ 0.001	m
Canard root chord length	$c_{r_{can}}$	0.06	$\pm$ 0.001	m
Canard tip chord length	$c_{t_{can}}$	0.05	$\pm$ 0.001	m
Canard lift coefficient derivative	C_{L_α}	2.86	$\pm$ 50%	rad^{-1}

* J_R and J_L vary during flight, and their profiles were exported from OpenRocket. The variation of $\pm$20% was applied to the full profile before importing into Simulink. This maintained the same variation during flight, but shifted it either up or down, depending on the value used for that simulation.

Appendix D – Canard Moment Diagrams

Figure 5 shows the geometry of the pitch and yaw canard configuration with respect to the CG, to aid with understanding the derivation of the dynamics equations in Chapter 3.

This diagram shows the x_1 canard. The x_2 canard is hidden behind the rocket body.

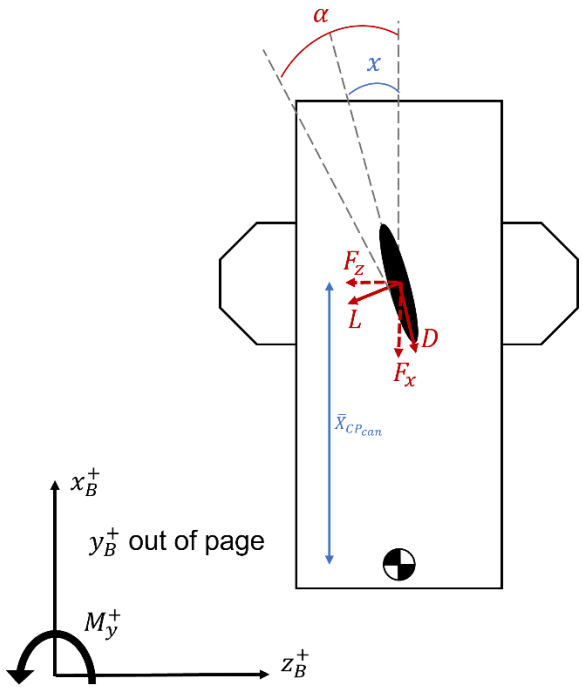

Figure 5 - Pitch / yaw canard configuration.

Figure 6 shows the configuration for the roll axis.

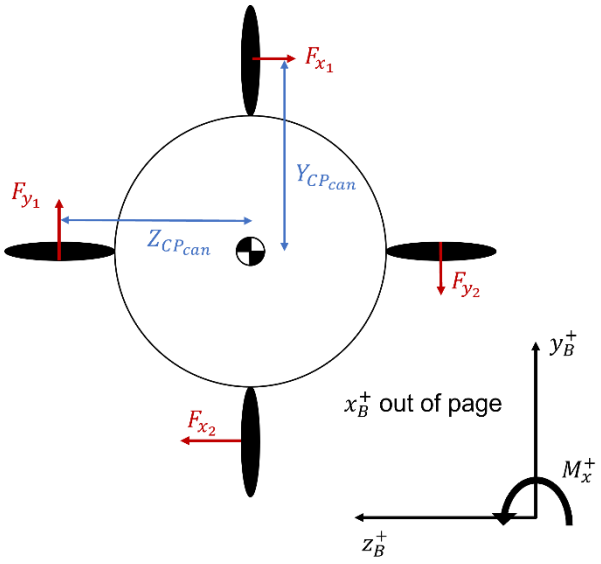

Figure 6 - Roll canard configuration.

Appendix E – Enhanced Wind Modelling Results

Figure 7 presents the system response to a varying crosswind both with and without the control system enabled. Dryden's continuous wind turbulence model was implemented in Simulink (MathWorks, n.d.), where both the speed and direction of the wind vector varies with the rocket's altitude and attitude.

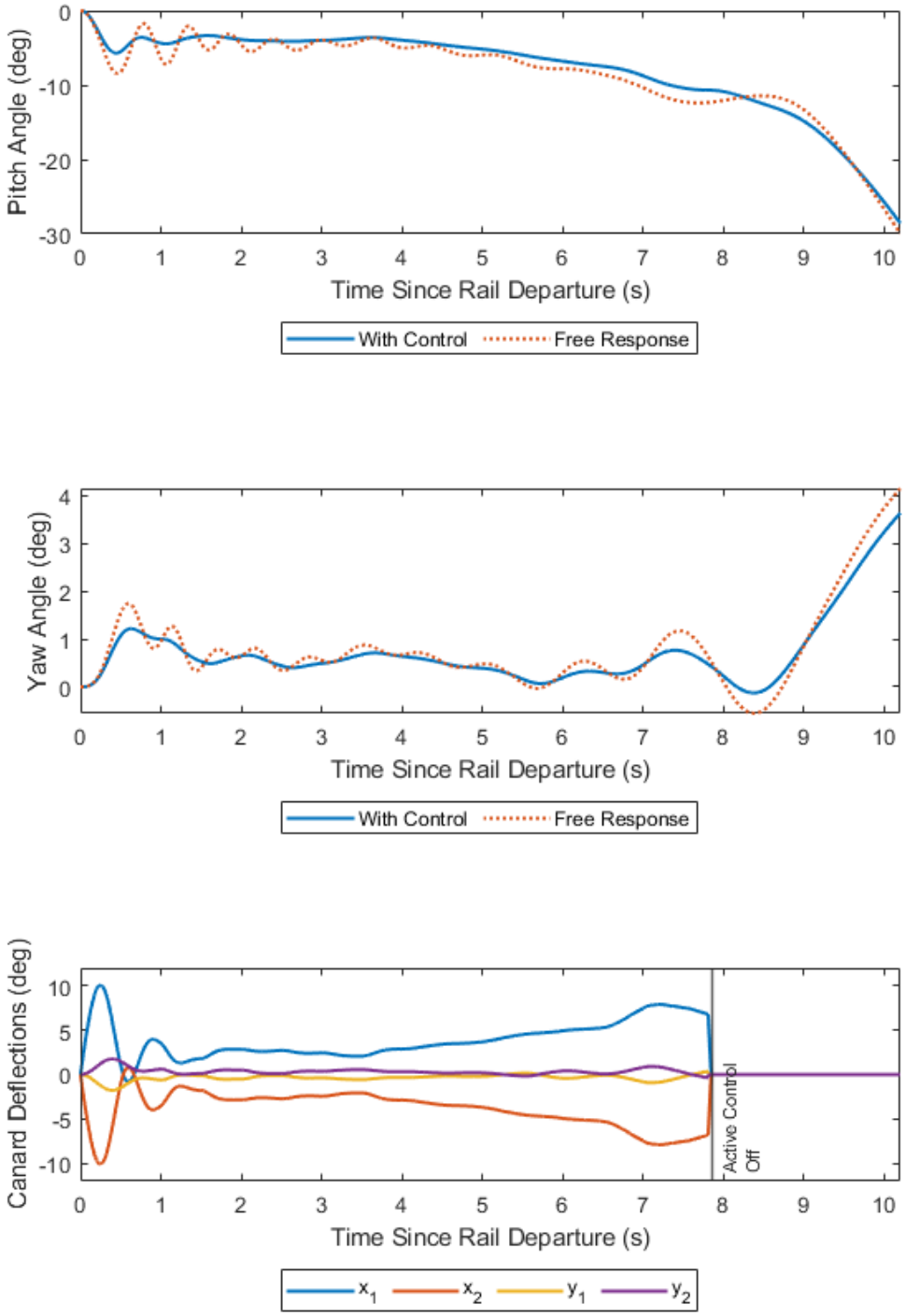

Figure 7 - System performance in response to a varying wind vector.